Magnetic shielding up to 0.67 T at 77 K using a stack of high temperature superconducting tape annuli of 26 mm bore

Sébastien Brialmont[1], Julien Dular[1], Laurent Wéra[1], Jean-François Fagnard[1], Benoît Vanderheyden[1], Christophe Geuzaine[1], Seungyong Hahn[2], Anup Patel[3] and Philippe Vanderbemden[1]

[1]Department of Electrical Engineering and Computer Science, University of Liège, Sart-Tilman, B-4000, Belgium

[2]Department of Electrical and Computer Engineering, Seoul National University, Seoul, South Korea

[3]AAC technologies, Edinburgh, UK

E-mail: S.Brialmont@uliege.be

December 2022

Abstract. In this work we demonstrate the magnetic shielding ability of a stack of $YBa_2Cu_3O_7$ (YBCO) tape annuli. The annuli are cut from a 46 mm wide second generation coated conductor deposited on a Ni-5at.%W alloy ferromagnetic substrate. The inner bore of the stacked tapes is 26 mm and the outer diameter is 45 mm. Three samples with different height (24 mm, 14.9 mm, 9.9 mm) are studied. All the experiments are carried out at both room temperature and liquid nitrogen temperature (77 K). The shielding efficiency is investigated when the magnetic field is applied either parallel to the axis of the stack (axial shielding) or perpendicular to it (transverse shielding). Under an axial field, magnetic shielding is found to be effective ($SF > 3$) up to magnetic flux densities of 0.67 T. The presence of the ferromagnetic substrates is found to have two important consequences. First, the stack of annuli is able to shield transverse flux densities in spite of its layered structure. Second, a finite magnetic shielding effectiveness is demonstrated at room temperature. In order to understand the contribution of the ferromagnetic substrates to the shielding mechanism, we use the experimental field dependence of the magnetic permeability as determined independently from hysteresis loop measurements on the same substrates. A finite-element homogenized model solved with an H-ϕ formulation is shown to successfully reproduce the shielding factor of the stack at room temperature and 77 K, both under axial and transverse applied fields. These models are also used to assess the influence of the critical current density and the magnetic permeability on the shielding efficiency. Finally, the results are used to predict the magnetic shielding properties of higher stacks, demonstrating their significant potential to shield axial fields of ~ 0.93 T (with $SF > 10$) at 77 K.

1. Introduction

Due to their ability to sustain large current densities without losses, superconducting materials can be used as efficient passive magnetic shields at low frequency [1, 2]. In a superconductor, passive magnetic shielding occurs through persistent current loops that generate a magnetic field opposing the applied magnetic field. In addition to their ability to achieve an ultra-low field environment [3–5], one of the main advantages of superconducting shields over conventional ones is that they are not limited by the saturation magnetisation of ferromagnetic materials (e.g. for mu-metal shields $\mu_0 M_{\rm sat} \sim 0.7$ T [6]). They can therefore operate at much higher flux densities [7–12]. This characteristic is a key element in the context of large scale superconducting devices generating flux densities of several teslas, e.g. rotating machines [13–16], magnetic lenses [17,18] or accelerator magnets, for which passive superconducting shields can be used to create a low field region [19–22] or to provide a screen to improve the magnetic field homogeneity [23].

Superconducting shielding can be successfully achieved using several materials, either low-temperature superconductors (LTS) [7, 8] or high-temperature superconductors (HTS). Among the latter, either (i) bulk materials or (ii) coated conductors can be used. The first category, bulk superconductors, exhibits constant progress in performance: magnetic shielding up to ~ 2 T at 4.2 K using MgB_2 [9], up to 1 T at 10 K using bulk $Bi_2Sr_2CaCu_2O_8$ [10], up to 1.5 T at 20 K using melt-textured $YBa_2Cu_3O_7$ [11] and recently, above 1.8 T at 20 K using MgB_2 [12], a material that can be machined [24] and fabricated in long tubes [25]. The magnetic shielding can be improved further when combining superconductors and ferromagnets [26–28]. If the magnetic shield is to be operated at 77 K, melt-textured (RE)$Ba_2Cu_3O_7$ (RE = rare earth) materials [29] enable shielding at the highest magnetic fields. One can currently achieve magnetic shielding up to 0.3 T – 0.4 T in volumes of ~ 1 cm^3 [30, 31], which is the current record at 77 K. Higher magnetic fields can be shielded but in tiny gaps of ~ 1 mm width [32]. The second category of interest includes shields made of 2nd generation (2G) coated conductor tapes. Since the shielding process relies on persistent shielding currents [33], the shield geometry should allow for a closed superconducting path, either across the width of the coated conductor [34–36], sometimes combined to bulk materials [37–39] or using 'eye-shaped' loops [40–42]. Moreover, the production of 2G coated conductor tapes has been significantly enhanced thanks to the so-called Rolling Assisted Biaxially Textured Substrate (RABiTS) as a template for depositing the HTS layer [43]. This technique typically uses Ni-W alloys which are weakly ferromagnetic [44, 45]. Even if ferromagnetic parts are generally undesired when dealing with coated conductor tapes - as they significantly increase the hysteresis and AC losses [46–48], such substrates can improve the magnetic shielding performance of the tapes [49]. In the past decade, exciting prospects have been opened with 'quasi-bulks' made of stacks of coated conductors [50–52]. If the stack is in the form of large annuli, it can be used as a compact 'persistent-mode' magnet for nuclear magnetic resonance (NMR) [53–55] or to produce large levitation forces [56]. Our group showed experimentally [57] that a stack of coated conductor annuli can also act as an efficient magnetic shield. Peng *et al.* [58] reported the 2D-axisymmetric modelling of the magnetic shielding behaviour of stacked coated conductors designed with various diameters, showing the significant potential of such stacks for shielding magnetic fields applied along the axis of the stack. The investigation of the magnetic shielding properties of such shields is now possible thanks to the development of 3D modelling techniques [59–61]. Systems combining superconducting (SC) and ferromagnetic (FM) materials in various geometries can be modelled efficiently either using a coupled $H-A$ formulation [62–64], or a homogenized model in which the SC and the FM materials are combined into one single material [65] taking into account the layered structure [66]. Such advances open the way to the 3D modelling of the magnetic properties of shields made of 2G coated conductor tapes deposited on a ferromagnetic substrate.

The purpose of the present work is to demonstrate experimentally the magnetic shielding ability of a stack of coated conductor annuli with large internal diameter (26 mm). The field is applied either along the axis of the stack (axial field) or perpendicular to it (transverse field, i.e. parallel to the plane of the tapes), as shown schematically in Figure 1. Since the coated conductors are deposited on a Ni-5at.%W RABiTS, the present work also aims at determining the possible benefits brought by their ferromagnetic substrate. Interestingly, the presence of a high-permeability substrate allows a conventional shielding mechanism to occur even above the critical

temperature of the superconductor. As a consequence, the properties of such a stack will be examined at both room temperature and at liquid nitrogen temperature (77 K). The set of experimental data, obtained on stacks of annuli of three different heights, will be compared to finite-element numerical modelling carried out either in 2D (axial configuration) or 3D (transverse configuration). This will allow us to investigate the respective influence of the superconducting properties, the ferromagnetic properties and the geometry of the shield.

2. Experimental set-up

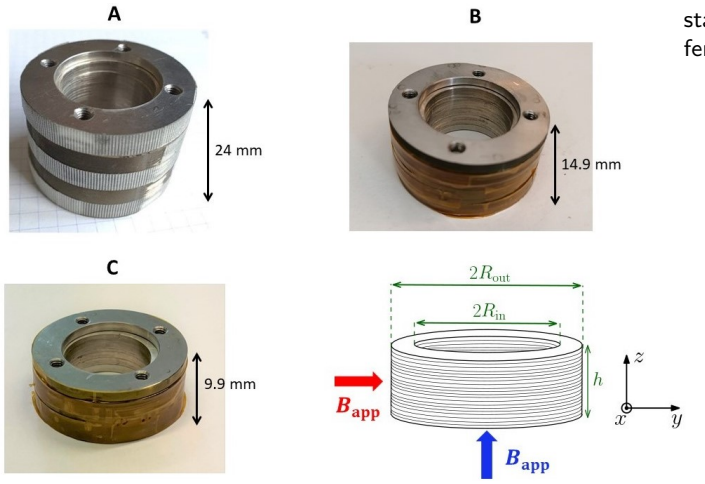

Figure 1: Pictures of the three shields A, B and C with their respective height and schematic illustration of the direction of the axial and transverse magnetic fields. Their complete geometrical characteristics are provided in Table 1.

The magnetic shield consists of a stack of YBCO tape annuli cut from a 46 mm wide coated conductor. The superconducting tape (manufactured by American Superconductor) is based on a rolling assisted biaxially textured Ni-5at.%W substrate (RABiTS) which is approximately 75 μm thick. The filling factor f, i.e. the volume fraction of ferromagnetic material in the stack, is $f \approx 0.92$. The HTS layer, made of $YBa_2Cu_3O_{7-d}$ has an approximate thickness of 1 μm and a nominal critical current between 200-350 A per cm width at self-field and 77 K (specified by the manufacturer). First, a central 26 mm hole was laser-cut in each tape [67]. Then, as described in a previous work [56], the surface of the loose square annuli was cut by spark erosion machining resulting in circular annuli of 45 mm outer diameter. Three magnetic shields of different heights are studied. The pictures of the three stacks of annuli as well as their dimensions are shown in Figure 1 and Table 1, respectively.

	Sample A	**Sample B**	**Sample C**
R_{in} [mm]	13	13	13
R_{out} [mm]	22.5	22.5	22.5
h [mm]	24	14.9	9.9
Number of tapes [-]	294	182	121
f [-]	0.92	0.92	0.92

Table 1: Characteristics and geometrical dimensions of the three stacks investigated. R_{in}, R_{out} and f respectively stand for the internal radius, the external radius and the ferromagnetic material filling factor.

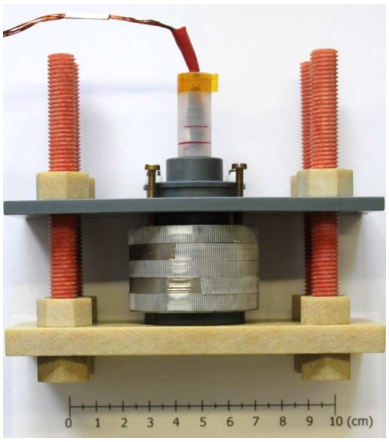

Figure 2: Experimental system for the measurement of the magnetic flux density inside the sample. The Hall probe is fixed so that the field is measured at the central position.

The magnetic shielding efficiencies of the stacks are investigated under an uniform magnetic field $B_{app} = \mu_0 H_{app}$ applied either parallel (axial configuration) or perpendicular (transverse configuration) to their axis at both 77 K and 293 K (room temperature). The magnetic field is measured inside the shield, at the central position with a three-axis Arepoc® Axis-3S Hall probe as shown in Figure 2 for Sample A. Calibration of the Hall probe at 77 K and room temperature was performed in a magnetic field generated by a copper solenoid coil. The resulting uncertainty on the magnetic field measurement was calculated to be of the order 2%. The shielding efficiency is characterized in terms of the dimensionless shielding factor defined as $SF = \frac{B_{app}}{B_{in}}$, where B_{in} is the magnetic flux density inside the sample and B_{app} is the uniform applied flux density.

3. Numerical modelling

Modelling systems combining high-temperature superconducting (HTS) and ferromagnetic (FM) materials is always challenging due to the strong non-linearities of the constitutive laws [63]. In this work, we use a 2D-axisymmetric model in the axial configuration and a 3D model in the transverse configuration. In both cases, the stack of coated conductors is modelled by replacing the detailed layered structure by a homogeneous hybrid (fictitious) material displaying both anisotropic ferromagnetic and superconducting properties [65]. This system is described by Maxwell's equations in the magnetodynamic (quasistatic) approximation [64, 68]:

$$\begin{cases} \text{div } \boldsymbol{B} = 0, \\ \text{curl } \boldsymbol{H} = \boldsymbol{J}, \\ \text{curl } \boldsymbol{E} = -\partial_t \boldsymbol{B}, \end{cases} \tag{1}$$

together with the constitutive equations $\boldsymbol{B} = \mu \boldsymbol{H}$ and $\boldsymbol{E} = \rho \boldsymbol{J}$. The quantities $\boldsymbol{B}$, $\boldsymbol{H}$, $\boldsymbol{J}$, $\boldsymbol{E}$, μ and ρ are respectively the magnetic flux density [T], the magnetic field [A/m], the electric current density [A/m^2], the electric field [V/m], the magnetic permeability [H/m] and the electrical resistivity [Ωm]. The model is solved with an $H - \phi$ formulation [63]. Due to the layered structure of the stack, the electric and magnetic constitutive laws of the homogeneous material are anisotropic. We first introduce the anisotropic relative permeability tensor [66]:

$$\boldsymbol{\mu_{an}}(H) = \begin{pmatrix} \mu_{x,y}(H) & 0 & 0 \\ 0 & \mu_{x,y}(H) & 0 \\ 0 & 0 & \mu_z(H) \end{pmatrix}, \tag{2}$$

with $\mu_{x,y}(H) = f\mu_r(H) + (1 - f)$ for the (x, y)-components and $\mu_z(H) = \frac{1}{\frac{f}{\mu_r(H)} + (1-f)}$ for the z-component, where f is the filling factor of the ferromagnetic material (defined in Section 2) and H is the average magnetic field. The (x, y, z)-coordinates system is shown in Figure 1. The field dependence of the relative permeability $\mu_r(H)$ of the ferromagnetic substrate was measured in a previous work on the same sample [69] at both room temperature and 77 K. For the modelling, we use an interpolation of the experimental relative permeability at each temperature: the corresponding data are plotted in Figure 3.

The homogenized model also involves an anisotropic resistivity tensor given by

$$\boldsymbol{\rho_{an}}(\boldsymbol{J}) = \begin{pmatrix} \rho(\boldsymbol{J}) & 0 & 0 \\ 0 & \rho(\boldsymbol{J}) & 0 \\ 0 & 0 & \rho_\infty \end{pmatrix}, \tag{3}$$

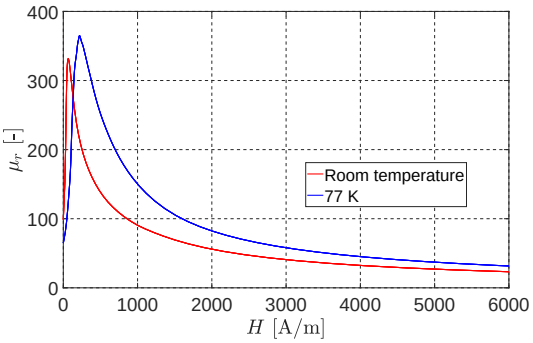

Figure 3: Magnetic field dependence of the magnetic relative permeability of the Ni-5at.%W ferromagnetic substrate measured on the investigated coated conductors. The results are obtained at both room temperature and 77 K.

where the quantity ρ_∞ is chosen as high as possible while avoiding numerical instabilities ($\rho_\infty = 0.01$ Ωm in practice) so the current does not flow in the axial direction. The resistivity $\rho(\boldsymbol{J})$ is defined as a function of the average current density $\boldsymbol{J}$ through the following power law [64, 70]:

$$\rho(\boldsymbol{J}) = \frac{E_c}{J_c(\boldsymbol{B})} \left(\frac{\|\boldsymbol{J}\|}{J_c(\boldsymbol{B})} \right)^{n-1}, \tag{4}$$

where the critical electric field and the dimensionless exponent are respectively fixed at $E_c = 10^{-4}$ V/m and $n = 20$. The model is implemented using a field-dependent critical current density $J_c(\boldsymbol{B})$ following Kim's law,

$$J_c(\boldsymbol{B}) = J_{c,0} \left(1 + \frac{\|\boldsymbol{B}\|}{B_0} \right)^{-1}, \tag{5}$$

where $J_{c,0} = 3.44 \times 10^8$ A/m^2 and $B_0 = 0.2$ T. The procedure followed to estimate these two parameters will be detailed in Section 5.1. Let us mention that the homogenized model assumes that the tapes composing the sample are much thinner than the typical mesh size (due to the high number of tapes). The critical current density described by Equation (5) is thus an averaged quantity over a high number of tapes in which the superconducting material is assumed to occupy a small fraction of the whole volume. Accordingly, the critical current density used in this model is largely underestimated compared to the actual critical current density of the superconducting layers. The numerical simulations are performed using the 'Life-HTS' toolkit [71] based on the open-source finite-element solver GetDP [72].

4. Results

4.1. Magnetic shielding at room temperature

In this section, the magnetic shielding is investigated at room temperature for the samples A, B and C in both axial and transverse configurations. Figure 4 shows the field dependence of the shielding factor SF measured at the central position of the stack. The experimental results are compared to numerical simulations carried out using the method and the material parameters described in Section 3.

We start by examining the experimental data for Sample A, appearing as plain lines in Figure 4(a). The first characteristic is that the stack exhibits a finite magnetic shielding (i.e. $SF > 1$) for both orientations. At low fields, the SF is found to be the highest in the transverse direction but decreases monotonically with the applied field. Oppositely, when the field is axial, the SF is rather small and almost field-independent.

In the transverse configuration, the monotonic decrease of the SF with B_{app} suggests that the shielding factor would be maximum when the applied field B_{app} goes to 0. However, at room temperature, Figure 3 shows that μ_r exhibits a maximal value in the very low field region ($H \sim 68$ A/m, corresponding to $B \sim 28$ mT in the ferromagnetic material) which also suggests that the SF curve should reach a maximum located around an external applied field $B_{\text{app}} \sim 3$ mT. This applied field yields a magnetic flux density inside the shield (B_{in}) below the noise level and the possible maximum of the SF curve cannot be verified experimentally. However, we can reasonably assume that the maximum SF occurs between the SF extrapolated at zero applied field (SF_0) and the first measurement data (SF_1). In a first approximation, the mean value between SF_0 and SF_1 should provide us with an adequate estimation of the maximal shielding factor. Doing so for both transverse and axial configurations, Figure 4(a) shows that Sample A is characterized by $SF \approx 35.67$ in the transverse configuration and $SF \approx 2.35$ in the axial configuration. As can be seen in Figures 4(b) and 4(c), the corresponding values for Samples B and C respectively are $SF \approx 10.2$ and $SF \approx 8.85$ in the transverse configuration, and $SF \approx 1.53$ and $SF \approx 1.25$ in the axial configuration. Since the superconductor does not contribute to the magnetic shielding at room temperature, the shielding factor is due to the ferromagnetic substrates only. The substrates appear to contribute mainly to shield the magnetic field component parallel to the tapes. The shielding efficiency depends directly on the aspect ratio of the sample. The results plotted in Figure 4 can be compared to estimations from analytical formulas derived by Mager and applicable

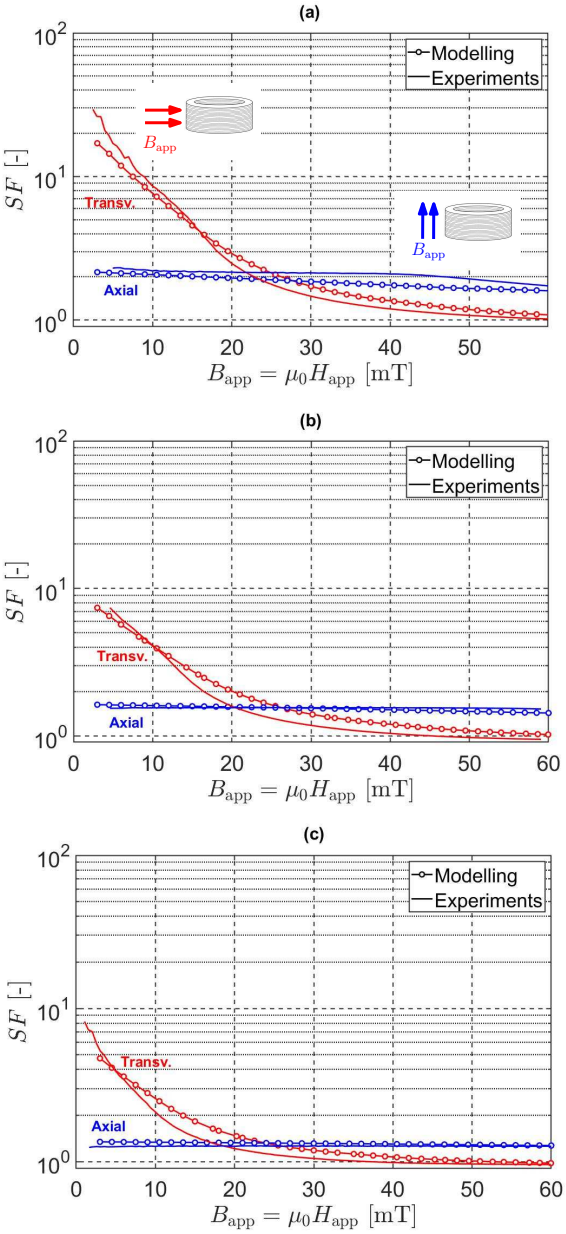

Figure 4: Shielding factor as a function of the applied magnetic flux density for (a) Sample A, (b) Sample B and (c) Sample C at room temperature. The experimental results are compared to numerical modelling in axial and transverse configurations. The field is applied at a rate of 0.75 mT/s.

to purely ferromagnetic cylindrical shields with a field-independent permeability [73, 74]. If we assume a homogenized anisotropic permeability of which axial and tangential components are respectively defined by [66]

$$\mu_{x,y} = f\mu_r, \tag{6}$$

$$\mu_z = \frac{1}{f/\mu_r + (1-f)}, \tag{7}$$

the shielding factor can be separated in two contributions: SF_{wall} standing for the field penetration across the cylinder wall, and SF_{open} standing for the field penetration through the open ends. In the transverse configuration, the two contributions are given by the following analytical formulas:

$$SF_{\text{wall}} = 1 + \frac{1}{4}\mu_{x,y}\left[1 - \left(\frac{R_{\text{in}}}{R_{\text{out}}}\right)^2\right], \quad (8)$$

$$SF_{\text{open}} = \frac{3}{2}e^{\left[3.832\left(\frac{h}{2R_{\text{in}}}\right)\right]}, \quad (9)$$

with R_{in} and R_{out} the internal and external radii respectively and h the height of the cylinder. In the axial configuration, the two contributions to the shielding factor are given by

$$SF_{\text{wall}} = 1 + 4N_z\left\{1 + \frac{1}{4}\mu_z\left[1 - \left(\frac{R_{\text{in}}}{R_{\text{out}}}\right)^2\right]\right\}, \quad (10)$$

$$SF_{\text{open}} = e^{\left[2.405\left(\frac{h}{2R_{\text{in}}}\right)\right]}\left[2.6\sqrt{\frac{h}{2R_{\text{out}}}}\right]^{-1}, \quad (11)$$

where N_z is the demagnetizing factor along the axis of the cylinder. The demagnetizing factors for cylinders can be found in Chen *et al.* [75]. We use here the magnetometric demagnetizing factor, leading to N_z = 0.4116 for Sample A, N_z = 0.5260 for Sample B and N_z = 0.614 for Sample C. The overall shielding factor, taking into account the flux penetration through the walls and through the open ends, is given by

$$\frac{1}{SF} = \frac{1}{SF_{\text{wall}}} + \frac{1}{SF_{\text{open}}}. \quad (12)$$

The results obtained by the Mager analytical formulas for Samples A, B and C are gathered in Table 2 for a magnetic relative permeability of μ_r = 332 which is the maximal permeability measured at room temperature. From the results shown in the table, we can conclude that the shielding factors obtained from the experimental measurements at low field are in a fair agreement with analytical formulas applicable to a purely ferromagnetic cylindrical shield. Such formulas, therefore, can be used to estimate, in a first approximation, the shielding factor of the stack of annuli at room temperature and low applied field. The comparison between SF_{wall} and SF_{open} shows that, for the dimensions equal to that of Sample A, the penetration of the magnetic flux in the cylinder is shared almost equally between the walls and the open ends, i.e. $SF_{\text{wall}} \sim SF_{\text{open}}$ for both orientations. When the height is decreased, as it is the case for Sample B and C, the flux penetration is mainly dictated by the open ends ($SF_{\text{open}} < SF_{\text{wall}}$). In order to model the decrease of the SF when the applied magnetic field is ramped from 0 to 60 mT, the field dependence of the magnetic permeability should be included. The numerical modelling, carried out following the procedure described in Section 3 including a field-dependent permeability, leads to the results shown in Figure 4. As can be seen, the numerical modelling is able to reproduce the field dependence of the experimental shielding factor with a nice agreement for both orientations.

(a)

	SF_{wall}	SF_{open}	SF	Exp. SF
Axial	5.96	4.85	2.67	2.35
Transv.	51.87	51.56	25.86	35.67

(b)

	SF_{wall}	SF_{open}	SF	Exp. SF
Axial	7.34	2.65	1.95	1.53
Transv.	51.87	13.48	10.69	10.2

(c)

	SF_{wall}	SF_{open}	SF	Exp. SF
Axial	8.4	2.05	1.65	1.25
Transv.	51.87	6.45	5.74	8.85

Table 2: Shielding factor estimation from the Mager analytical formulas [73, 74] for (a) Sample A, (b) Sample B and (c) Sample C. The results are obtained for a maximum relative magnetic permeability of μ_r = 332, assumed to be field-independent.

4.2. Magnetic shielding at 77 K

We now investigate the shielding at 77 K in order to assess the effect of the HTS layers on the shielding efficiency. Figure 5 shows the field dependence of the shielding factor under either an axial or a transverse field as well as a comparison with numerical modelling (using $J_{c,0} = 3.44 \times 10^8$ A/m^2 and $B_0 = 0.2$ T for the $J_c(\boldsymbol{B})$ law as described in Section 3) for the samples A, B and C. As can be seen in Figure 5(a), in the axial configuration and in the considered field range ($B_{\text{app}} < 60$ mT), an almost field-independent shielding factor is obtained for Sample A ($SF \approx 45$). The value of SF is much bigger than at room temperature due to the contribution of the shielding current loops flowing in the HTS layers. Under a transverse applied field, i.e. parallel to the HTS layers, we expect their contribution to be negligible at first order. The transverse magnetic shielding, therefore, is mainly due to the ferromagnetic substrates. The results of Figure 5 show that the ferromagnetic layers

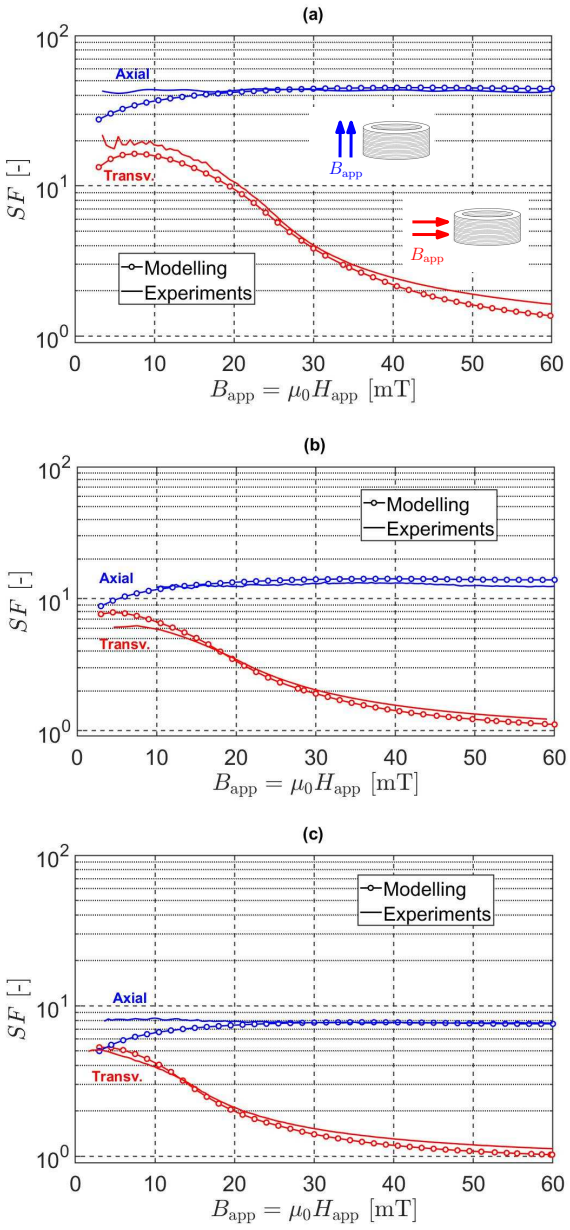

Figure 5: Shielding factor as a function of the applied magnetic flux density for (a) Sample A, (b) Sample B and (c) Sample C at 77 K. The experimental results are compared to numerical modelling in axial and transverse configurations. The field is applied at a rate of 0.75 mT/s.

give rise to a significant transverse shielding factor ($SF \approx 20$ for Sample A), despite the layered structure. The transverse shielding factor, however, is always lower than the axial one in the considered field range. The SF first exhibits a plateau (or a very smooth bump) and then, decreases monotonically. Similar conclusions can be drawn for Samples B and C (Figures 5(b) and 5(c)) except that the shielding factor values are lower than for Sample A due to their lower height. The results obtained by numerical modelling, shown in Figure 5, are found to be in excellent agreement, both qualitatively and quantitatively, with the experimental results for the axial and transverse orientations. Note that the lowest external applied fields in Figure 5 are below the first critical field value $\mu_0 H_{c,1} \approx 6.5$ mT determined experimentally for an YBCO crystal at 77 K [76]. The fact that parts of the shield may be below $H_{c,1}$ – in which the constitutive laws (4) and (5) are not valid since they apply to a superconductor in the mixed state [77] – cannot be ruled out and may explain the difference between the modelled and experimental data at low fields. In the current stacked tape geometry, however, it is believed that strong demagnetization effects arising at the edges of the superconducting films may lead to fields exceeding $H_{c,1}$ locally. For a densely piled stack of tapes subjected to an applied field H_{app} perpendicular to the surface of the tapes, analytical calculations show that the local field H at the edge of the stack can be approximated as $H \approx 3/2 H_{app}$ [78]. Moreover, due to possible surface roughness and irregularities, the field along the edges of the tapes may be concentrated locally so that the flux can penetrate at applied fields lower than $H_{c,1}$ [79]. Further local field concentration effects are expected to arise because of the presence of the high permeability, ferromagnetic substrate, leading to flux density inside the superconducting material to be larger than $\mu_0 H_{c,1}$.

In addition to the data above, all measured at the centre of the shield, it is interesting to look at the evolution of the shielding efficiency along the axis of the shield. Figure 6 shows the measured and modelled axial shielding factor along the z-axis inside the samples A and B at $T = 77$ K, for a 60 mT axial applied field. As expected, the highest shielding factors are obtained in the region around the central position ($z = 0$ mm). The experimental results obtained for Sample A happen to be slightly dissymmetric around the central position. This dissymmetry can be explained either by the uncertainty on the vertical position of the probe during the measurement process or by a non-uniform distribution of the critical currents of the coated conductors composing the sample, and will not be discussed further. By construction, the numerical model is perfectly symmetric with respect to the $z = 0$ plane. This perfect symmetry may be in contrast with the properties of the actual samples consisting of a layered and thus potentially dissymmetric structure. The results plotted in Figure 6 show that the numerical modelling is able to reproduce the distribution of the shielding factor inside the stack. Interestingly, it is found that in the vicinity of the open ends ($z = \pm h/2$), a shielding factor $SF \sim 6$ is observed for both geometries. Going from the open end towards the centre of

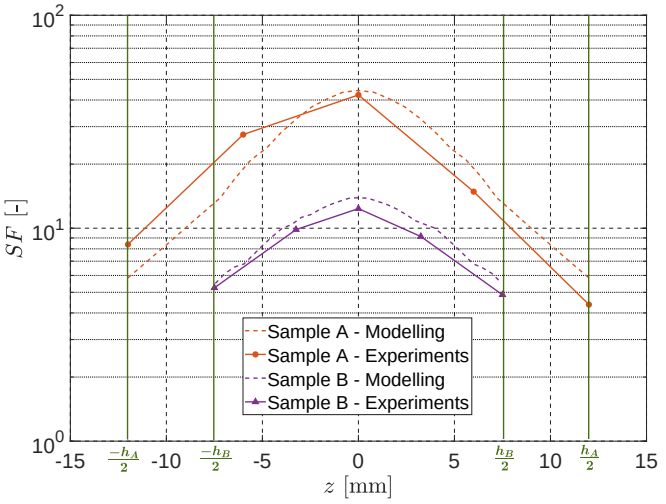

Figure 6: Shielding factor as a function of the position on the z-axis inside the sample for an axial applied field of 60 mT. Comparison between modelling and experimental results for Sample A and Sample B at 77 K. The central position corresponds to $z = 0$ mm. The vertical green lines show the position of the open ends for the two samples, $\pm h_A/2$ for Sample A and $\pm h_B/2$ for Sample B.

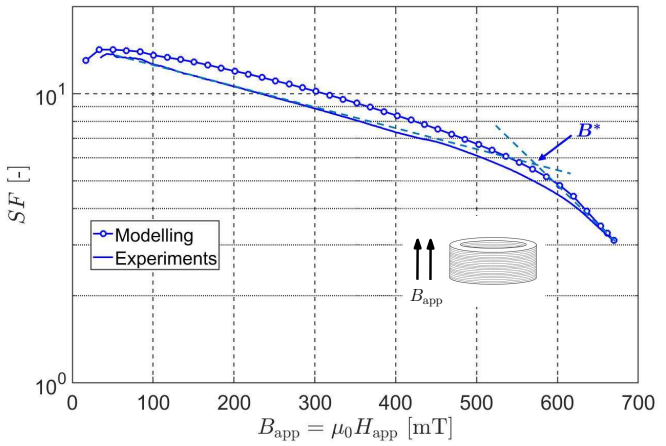

Figure 7: Shielding factor as a function of the axial applied magnetic flux density for Sample B. Comparison between experimental and modelling results. $T = 77$ K. The field is applied at a rate of 5 mT/s. The measurements are obtained at the center of the shield.

the sample, the shielding factor is found to increase almost exponentially with the distance z' from the open end, as evidenced from the quasi-linear behaviour observed in the semi-log scale of Figure 6. Such an exponential increase is also expected for type-I superconductors [80].

In order to investigate the behaviour of the shield at larger fields, the shielding factor was also measured under an axial applied field up to 670 mT on Sample B (Sample A was no longer available by the time of these measurements). The field dependence of the shielding factor, measured at the center of the shield, is shown in Figure 7 and is found to decrease monotonically with the applied field. From these measurements, it is possible to obtain a rough estimation of the critical current density as will be shown in the next section.

5. Discussion

In this section, we examine in more details how the results obtained in Section 4 can be used to determine the critical current density of the stack (5.1), to predict the behaviour of higher stacks (5.2) and to understand how the shielding factor is influenced either by the $J_c(B)$ of the superconductor or the $\mu_r(B)$ of the ferromagnet (5.3).

5.1. Determination of the J_c of the stack

In order to determine the critical current density of the superconductor from the magnetic shielding measurements, we use the data plotted in Figure 7, obtained for an axial applied field ($B_{\text{app}} \parallel z$). Due to the layered structure, there is no superconducting current flowing along the axial direction. By symmetry, we can also assume that there is no shielding current flowing in the radial direction. Moreover, under an axial field at 77 K, it is expected that the magnetic shielding contribution of the magnetic substrates is very low compared to the contribution of the superconducting layers. Therefore, in a first approximation, one can assume that the magnetic shielding at 77 K is caused by azimuthal currents flowing in the individual superconducting layers only. From a macroscopic point of view, this is equivalent to having a plain superconductor (with no ferromagnetic substrate and no gap between the superconducting layers) in which a bulk, macroscopic, azimuthal "engineering" critical current density J_e can flow. Figure 7 shows that the axial shielding factor first decreases smoothly with the applied field before going through a more abrupt decrease after 500 mT. We show below that this steeper decrease is related to the applied field under which the sample is fully penetrated. More precisely, the abrupt decrease gives rise to a slope break in the $SF(B)$ measurement, spotted by the flux density value B^* in Figure 7. For Sample B, this value is approximately equal to $B^* \approx 568$ mT.

It is of interest to investigate whether this B^* value is proportional to the full penetration field of the sample B_{pen}, i.e. whether one has $B^* = KB_{\text{pen}}$,

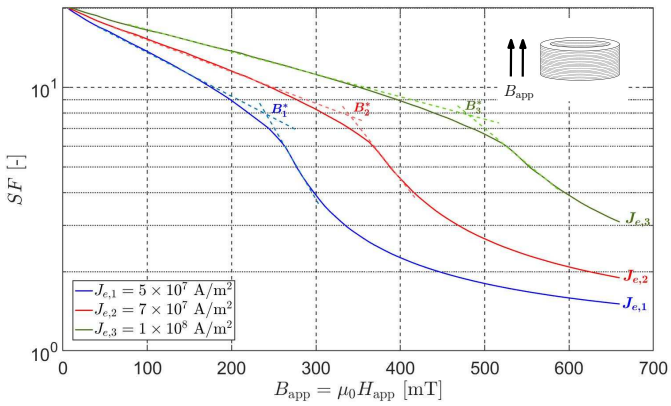

Figure 8: Field dependence of the SF obtained by a 2D-axisymmetric modelling of a bulk superconducting cylinder with the same geometrical dimensions than Sample B. The results are obtained for three different values of constant J_e. $T = 77$ K.

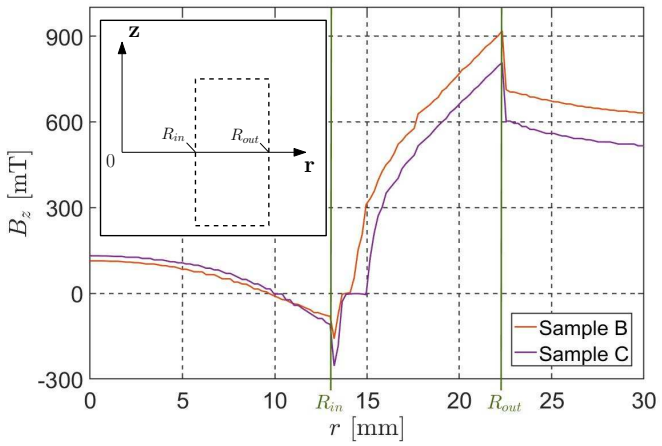

Figure 9: Numerical modelling of the z-component of the magnetic flux density as a function of the radial distance r from the center of the cylinder. The flux density over r is obtained for both Sample B and Sample C when the applied field is equal to B^* (568 mT for Sample B and 479 mT for Sample C).

where K is a constant. In the assumption of a field-independent current density, B_{pen} is given by the following formula [81]:

$$B_{\text{pen}} = \mu_0 J_e d \left(\frac{h}{4\bar{R}}\right) \ln\left(\frac{4\bar{R}}{h} + \sqrt{1 + \left(\frac{4\bar{R}}{h}\right)^2}\right), \quad (13)$$

where $\bar{R}$, h and d are respectively the mean radius, the height, and the wall thickness of the cylinder.

In order to determine K, a simple 2D-axisymmetric model of a bulk purely superconducting cylinder with the geometrical dimensions of Sample B was used. The model was solved with an $H - \phi$ formulation. Figure 8 shows the field dependence of the shielding factor for three constant engineering critical current densities - within the plausible range that can be expected - for which the slope break can be graphically determined. Let us note that in this particular case, the engineering critical current density J_e is equal to the critical current density J_c as we model a bulk HTS cylinder. We obtain $B_1^* \approx 238$ mT , $B_2^* \approx 334$ mT and $B_3^* \approx 475$ mT respectively yielding to $K_1 \approx 0.839$, $K_2 \approx 0.841$ and $K_3 \approx 0.837$. From this analysis, we can conclude that the factor K is independent of the critical current density in the range of J_c considered. If we take the average of these values, we obtain $K_{\text{avg}} \approx 0.839$. Hence, using the formula (13), the average, engineering critical current density can be approximated from the measurement of B^* and the knowledge of the factor K as well as the sample geometry. The same procedure was applied on the sample C and the results for the two samples are compared in Table 3. Accordingly, even if this procedure is rather arbitrary, it leads to a rough estimation of the engineering critical current density which happens to be weakly dependent on the sample geometry.

	B^*	K_{avg}	J_e
Sample B	568 mT	0.839	1.19×10^8 A/m^2
Sample C	479 mT	0.842	1.28×10^8 A/m^2

Table 3: Comparison of the experimental slope break B^*, the averaged K factor and the engineering critical current density J_e, assumed to be field-independent for two different aspect ratios.

The modelling results obtained with a field-dependent critical current density described by Equation (5) of the axial shielding up to 670 mT are shown to be in a rather good agreement with the experimental results as we can see in Figure 7. In order to justify the numerical values used for the two parameters $J_{c,0}$ and B_0 appearing in Equation (5), we can show that they lead to consistent values compared to those depicted in Table 3. The parameter $J_{c,0}$ is estimated by using the data provided by the manufacturer. As mentioned in Section 2, the critical current at self field is 200-350 A by cm width. Taking the average value of 275 A/cm and assuming that the current flows in the entire cross section, the engineering critical current density can be easily calculated. Taking a tape thickness of 80 μm, we obtain $J_{e,0} = 3.44 \times 10^8$ A/m^2. This value is then used for the first parameter of Kim's law, $J_{c,0}$. From this, the parameter B_0 can be estimated by finding the value leading to the best fit between the experimental and numerical data. This yields $B_0 = 0.2$ T. This set of parameters $(J_{c,0}, B_0)$ leads to the modelling results

shown in Figure 7. In order to check if the parameters of the $J_c(\boldsymbol{B})$ law make sense, the value of J_c should be consistent with the engineering critical current density values in Table 3 obtained at an applied flux density of $B_{\text{app}} = B^*$. Figure 9 shows the 2D modelling of the magnetic flux density component perpendicular to the tapes along the radial direction (as illustrated in the inset) when the external applied field is equal to B^*. The figure shows the flux density inside the sample B and the sample C. Therefore, the two sets of data are obtained for two different values of applied flux densities ($B^* = 568$ mT for Sample B and $B^* = 479$ mT for Sample C). As can be seen in Figure 9, the flux density strongly varies between the internal and the external walls of the cylinder and so does the critical current density. If we consider, in a first approximation, that the field is perpendicular to the tapes, the flux density B in the superconducting layer is equal to that in the ferromagnetic layer and Kim's law (5) becomes:

$$J_c(\boldsymbol{B}) = J_c(B_z) = J_{c,0}\left(1 + \frac{|B_z|}{B_0}\right)^{-1}. \qquad (14)$$

Knowing the values of B_z from Figure 9, we can compute the value of $J_c(B_z)$ along r for Sample B and Sample C. The average values of the critical current density computed between R_{in} and R_{out} are $J_c \approx 1.17 \times 10^8$ A/m^2 for Sample B and $J_c \approx 1.4 \times 10^8$ A/m^2 for Sample C. These values are found to be fully consistent with the experimental engineering critical current densities depicted in Table 3 and give confidence in the determination of the parameters of the $J_c(\boldsymbol{B})$ law from the magnetic shielding measurements.

5.2. Prediction of the shielding behaviour of higher stacks

In the following, we investigate the effect of the height of the sample on the magnetic shielding performances. As the results plotted in Figure 7 show a good agreement between the 2D-axisymmetric homogenized model using a field-dependent critical current density and the experimental measurements under an axial field value up to 670 mT, this model can then be used to assess the field dependence of the shielding performance for samples with higher dimensions. Figure 10 shows the modelled shielding factor as a function of the applied axial field for three samples of different heights. From this figure, the slope break characteristic of the sample full penetration appears not to depend strongly on the height of the sample. Indeed, for a sample of height $h = 24$ mm, the slope break is observed at an applied axial flux density of approximately 700 mT. For samples of height $2h$ and $3h$, the slope breaks occur at approximately 748 mT and 812 mT respectively. Figure 10, however, clearly

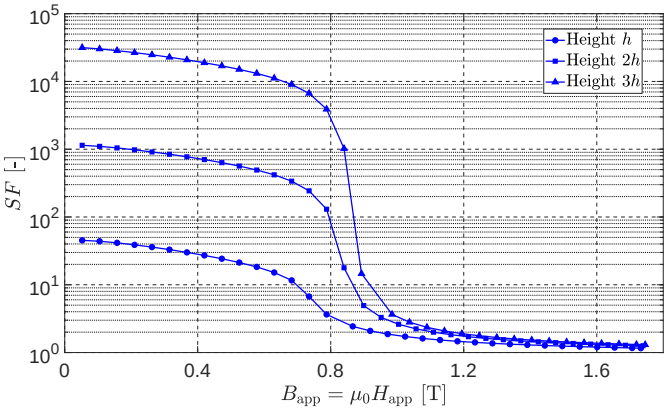

Figure 10: Shielding factor as a function of flux density applied in the axial direction for three different sample's height. Here $h = 24$ mm. The internal and external radii are the same than for Samples A, B and C. The results are obtained at 77 K. The field is applied at a rate of 5 mT/s.

shows that the height has a significant impact on the value of the shielding factor itself. At lower fields ($B_{\text{app}} < 200$ mT), a sample with a height equal to $h = 24$ mm can reach a $SF \sim 45$ (see Figure 5(a)), whereas a sample three times higher can reach a shielding factor $SF > 30000$. Above $B_{\text{app}} \approx 1$ T the shielding factor drops to values smaller than $SF = 3$ whatever the height of the stack. The practical consequence of a significant dependence of the shielding factor as a function of the aspect ratio - as is the case for bulk superconductors - is that the field at which the SF reaches a given user-defined threshold, e.g. $SF = 10$, increases noticeably with increasing height. In the present case, these values are 0.7 T, 0.876 T and 0.931 T for stacks of height h, $2h$ and $3h$ respectively. This shows the potential of such stacks of tapes to shield fields up to ~ 0.9 T at 77 K.

5.3. Effect of J_c and μ_r on the shielding efficiency

When the magnetic shield is operated at 77 K, the shielding results from a combined action of the superconducting layers and the ferromagnetic substrates, both of which being characterized by field-dependent parameters. In this section, we investigate in more details the effect of the superconducting layers and the ferromagnetic substrates on the magnetic shielding under either an axial or a transverse applied field.

First, the effect of the critical current density on the shielding efficiency is studied. Figure 11 compares the shielding factor modelled with a field-dependent critical current density $J_c(B)$ given by Equation (5), with the SF modelled with a constant J_c (5×10^7, 1.2×10^8 and 2×10^8 A/m^2) arbitrarily

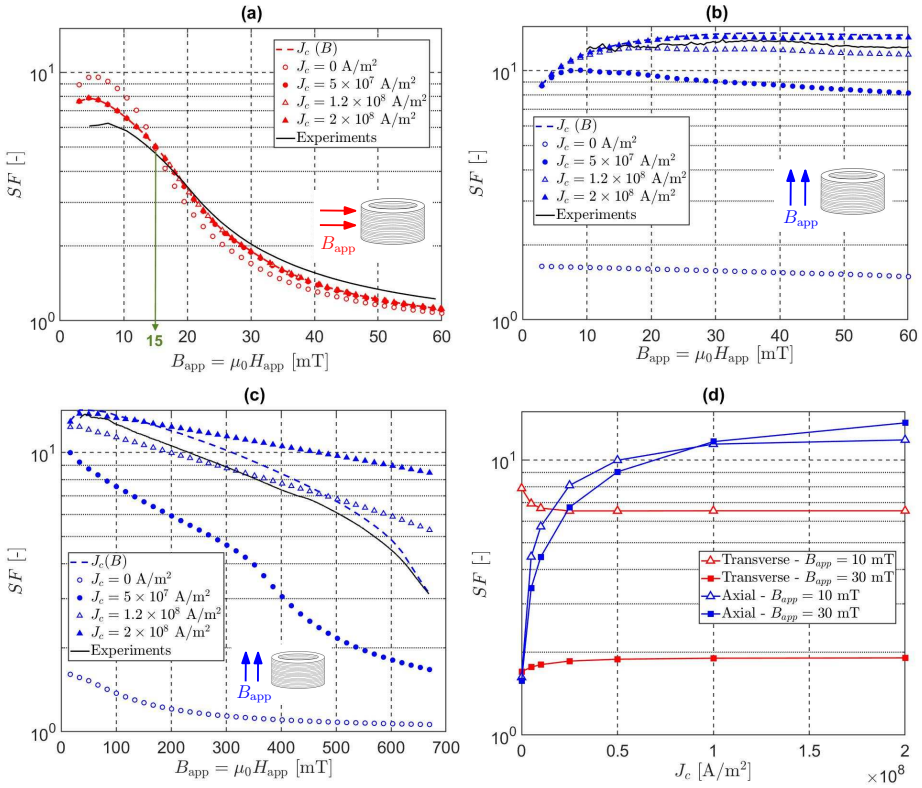

Figure 11: Comparison between experimental and numerical modelling results of the shielding factor with different values of J_c using a field-dependent permeability $\mu_r(B)$. The considered stack is Sample B. The shielding factor is plotted in (a) transverse configurations under a field range < 60 mT, (b) axial configurations under a field range < 60 mT and (c) in axial configuration under a field range up to 670 mT. The vertical arrow in graph (a) is used to indicate the crossover between the curves modelled with or without superconductor ($J_c = 0$). The graph (d) shows the modelled shielding factor as a function of J_c at two applied fields (10 mT and 30 mT). The temperature is 77 K.

chosen around the experimental estimation obtained in Section 5.2 ($J_e \approx 1.2 \times 10^8$ A/m^2), or with no superconductor ($J_c = 0$ A/m^2). The modelling results are also compared with the experimental data. Here, we consider only Sample B and all the results are obtained using a field-dependent permeability $\mu_r(B)$. Figure 11(a) shows the shielding factor measured for a transverse field. As can be seen, within the range of investigated values, the modelled field dependence of the shielding factor is found to follow a qualitative behaviour that is independent on the value of J_c: a smooth bump followed by a monotonic decrease. Interestingly, the low-field ($B_{\rm app} < 15$ mT) SF that would be measured without superconductor is slightly higher than when the superconductor is present, while the opposite behaviour is observed above 15 mT. These results underline that the superconducting layers have a minor effect on the shielding process in the transverse configuration, but that this effect is not zero. More precisely, at low field, the bending of the magnetic flux lines caused by the ferromagnetic substrates leads to a non-zero axial component B_z which, in turn, generates shielding currents in the superconducting layers. In particular, for $B_{\rm app} < 15$ mT, the shielding process is mainly due to the ferromagnetic material in which the flux lines are channelled following the path of least magnetic reluctance. With the presence of superconducting material ($J_c \neq 0$ A/m^2), the shielding currents induced in the superconductor because of the non-zero B_z, oppose to the applied field. Hence, they increase the global magnetic reluctance and prevent the magnetic flux lines from being properly channelled by the ferromagnetic material. At the center of the cylinder, this phenomenon results in a transverse shielding factor smaller than that predicted in the absence of superconductor ($J_c = 0$ A/m^2) obtained at the center of the cylinder. When no superconducting material is present, however, the ferromagnetic material saturates more rapidly (i.e. the permeability decreases with increasing magnetic flux density channelled within the sample). At an applied field $B_{\rm app} > 15$ mT, the shielding efficiency is thus slightly improved by the presence of shielding currents ($J_c \neq 0$). In spite of this effect, the results plotted in

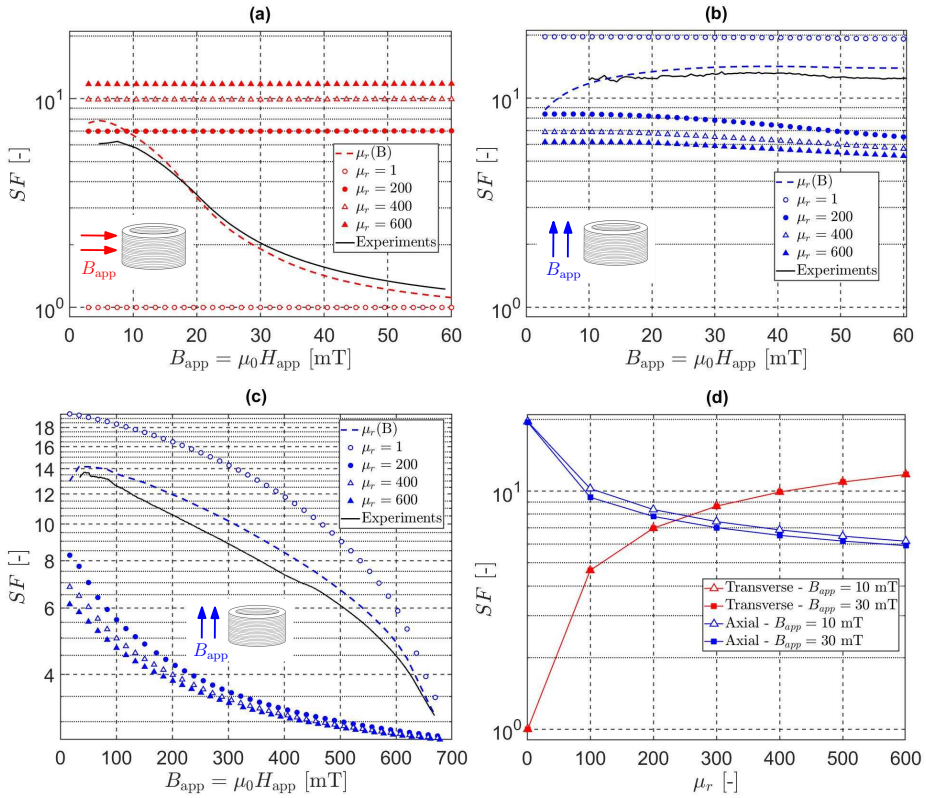

Figure 12: Comparison between experimental and numerical modelling results of the shielding factor with different values of μ_r using the field dependence of the critical current density $J_c(B)$ given by (5). The stack considered is Sample B. The shielding factor is plotted in (a) transverse configurations under a field range < 60 mT, (b) axial configurations under a field range < 60 mT and (c) in axial configuration under a field range up to 670 mT. The graph (d) shows the modelled shielding factor as a function of μ_r at two applied fields (10 mT and 30 mT). For the transverse configuration (data shown in red), the results obtained at 10 mT and 30 mT are exactly superimposed.

The temperature is 77 K.

Figure 11(a) give evidence that the shielding process is mainly due to the ferromagnetic substrate and emphasize the benefits of Ni-W alloys for a magnetic shielding application. We now turn to the behaviour of the shield subjected to an axial field. In the range $B_{\rm app} < 60$ mT (Figure 11(b)), considering a constant J_c in the axisymmetric model does not change significantly the shape of the field dependence of the shielding factor. In this magnetic field range, the experimental data are within the modelled curves for a constant $J_c = 10^8$ A/m^2 and $J_c = 2 \times 10^8$ A/m^2. This is no longer true for higher fields (Figure 11(c)) for which the impact of the value of the constant critical current density becomes more and more important as the axial field increases. A critical current $J_c = 2 \times 10^8$ A/m^2 clearly overestimates the shielding factor at the highest fields. These results point out the interest of using a simple field-dependent $J_c(B)$ in the model as described in Section 3. It is worth mentioning that when we consider a zero J_c, the axial shielding factor keeps a value > 1 (~ 1.6 at low field, then monotonically decreasing) due to the weak effect of the magnetic substrates on the magnetic shielding. The maximum SF value at low field is comparable to that measured at room temperature (~ 1.5) since the flux penetration mainly occurs through the open ends in this regime. Consistently with the previous results, Figure 11(d) shows how the modelled shielding factor at two different applied fields (10 mT and 30 mT) changes as the critical current density increases from 0 to 2×10^8 A/m^2. This figure shows the increase of the shielding factor with the critical current density at a fixed applied axial field. This is due to the increase of the shielding current density in the superconducting layers. In the axial regime, we also observe that the SF first increases sharply with the J_c and then saturates. The saturation is slower and occurs at a higher SF at $B_{\rm app} = 30$ mT than at $B_{\rm app} = 10$ mT. Under a transverse applied field, Figure 11(d) shows the small variation of the SF with the critical current density

in the very low J_c regime (as already discussed above in this paragraph). For higher J_c, the curves exhibit no variation of the shielding factor with the critical current density at all.

Finally, we investigate the effect of the magnetic permeability of the substrate, and compare a constant μ_r to a field-dependent permeability $\mu_r(B)$ considering the field dependence of the critical current density $J_c(B)$ given by (5). Modelling results of the shielding factor of Sample B considering a field-dependent permeability or a constant permeability under an axial field are compared in Figure 12(a) in the field range $B_{\text{app}} < 60$ mT. The constant permeability values in our analysis are chosen arbitrarily around the maximum μ_r observed in Figure 3 at 77 K ($\approx$ 365). When the magnetic permeability is fixed to a constant value, the transverse shielding factor is shown to be field-independent in this field range. This remains consistent with the fact that the transverse shielding is mainly due to the ferromagnetic substrates. We also observe that the constant shielding factor increases with the constant magnetic permeability, as also shown in Figure 12(d) which displays the SF vs. μ_r dependence for two given applied fields $B_{\text{app}} = 10$ mT and $B_{\text{app}} = 30$ mT. Such a behaviour is in agreement with the theoretical behaviour that can be expected from Equations (8) and (9) that are valid for a purely ferromagnetic shield. When a field–dependent permeability $\mu_r(B)$ is considered, the SF is found to decrease with the applied field monotonically up to 60 mT. This result may look paradoxical since $\mu_r(B)$ at 77 K increases in this field range [69], corresponding also to the increasing part of the permeability vs. magnetic field in the ferromagnetic substrates $\mu_r(H)$ curve shown in Figure 3. The explanation comes from the fact that the (non-uniform) magnetic flux density inside the FM when the stack is used to shield an applied transverse field H_{app} might be higher than the uniform flux density $B_{\text{app}} = \mu_0 H_{\text{app}}$. When $B_{\text{app}} > 15$ mT the flux density in the material globally exceeds 100 mT. As a result, when the applied field is in the range 15 mT $< B_{\text{app}} <$ 60 mT, most of the material is located on the descending part of the $\mu_r(B)$ dependence reported in [69]. This justifies the decreasing SF shown is Figure 12(a). When the model does not take the ferromagnetic material into account ($\mu_r = 1$), we do not observe any shielding effect at all in the transverse case, as expected intuitively. Under an axial applied field (Figure 12(b)), the results show that modelling the shielding factor by taking a field-dependent permeability as described in Section 3 for the ferromagnetic substrates is fully justified to fit properly the experimental results. When the field is applied in the axial direction, the shielding efficiency increases as the magnetic permeability decreases and we obtain a maximal magnetic shielding in the case where $\mu_r = 1$. This is also observed under an applied field up to 670 mT (Figure 12(c)). This behaviour can be explained by two elements. First, under the presence of a ferromagnetic material, the flux lines are attracted; the amplitude of the axial component of the flux density inside the sample, and thus inside the HTS layers, is increased. If the material is modelled using a field-dependent J_c, this increase of the flux density will result in a reduced critical current density and then a reduced shielding efficiency. Figure 13 shows the distribution of the shielding current density over the section of the sample under an applied external field $B_{\text{app}} = 200$ mT for different values of magnetic permeabilities. The results shown in this figure are obtained using a 2D-axisymmetric model with a field-dependent critical current density following Equation (5). The effect of the variation of the critical current density clearly appears in this figure which shows that the shielding currents are reduced when using a permeability $\mu_r > 1$ compared to those obtained in the case where no

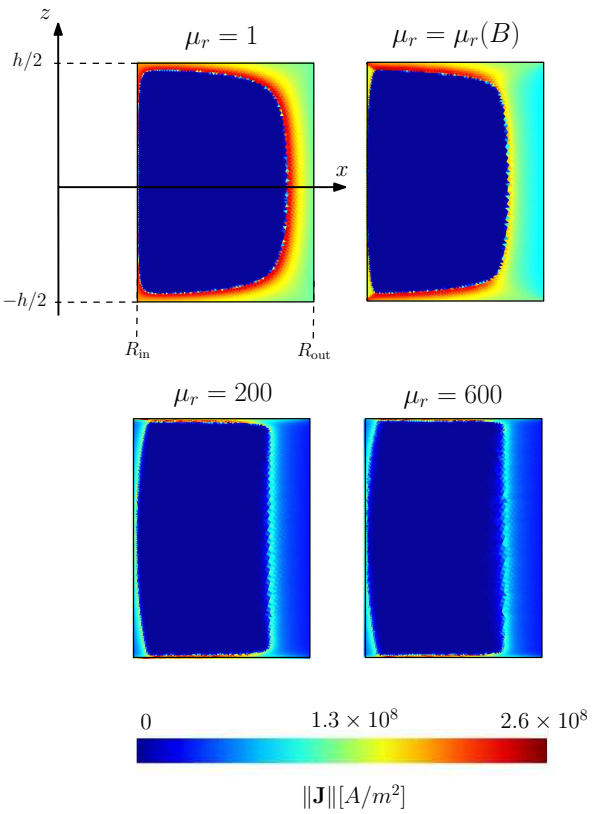

Figure 13: Shielding current density distribution on the section following the (x, z) plane for different values of anisotropic relative permeabilities under an applied axial field of 200 mT. The results are obtained with a model using the $J_c(B)$ dependence (5). The geometry used is that of Sample B.

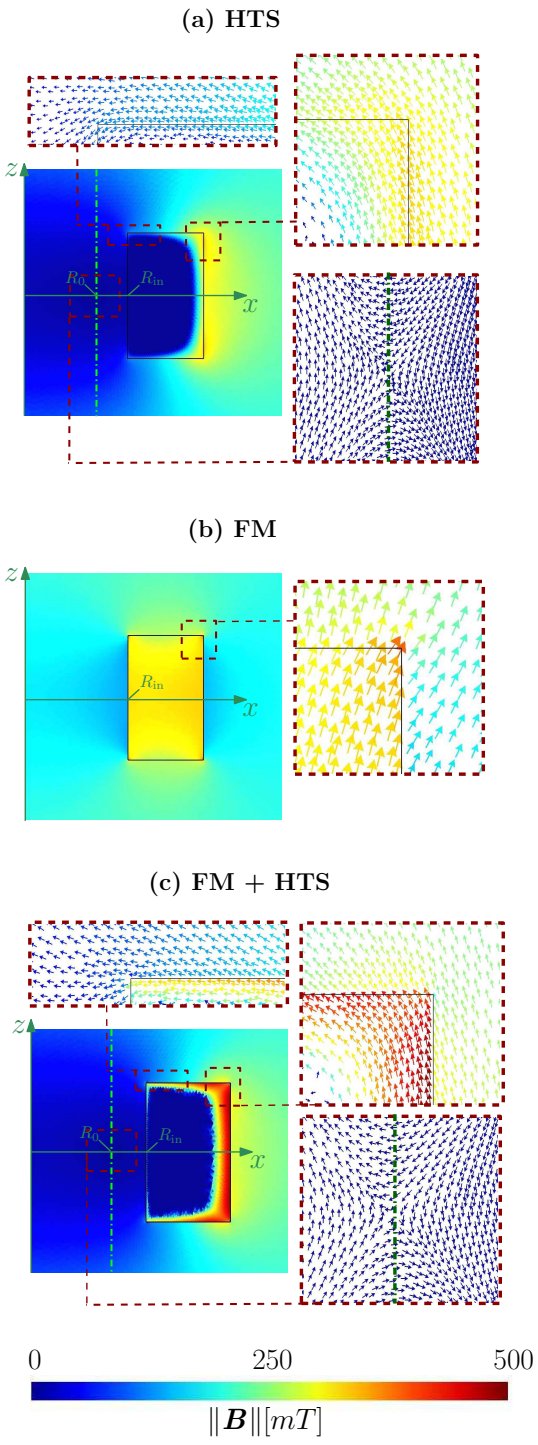

Figure 14: Distribution of the magnetic flux density $\|\boldsymbol{B}\|$ and magnetic flux lines in the (x, z) plane for an axial applied field of 200 mT. The flux density distribution is shown for a shield consisting of (a) only superconducting material (HTS), (b) only ferromagnetic material (FM) and (c) a combination of ferromagnetic (92%) and superconducting (8%) material (FM+HTS). The dash-dotted green line in (a) and (c) spots the zero-B_z region. The geometry used is that of Sample B.

ferromagnetic material is considered ($\mu_r = 1$). Figure 13 also shows that the shielding currents are weakly affected by the permeability in the range $\mu_r = 200$ to 600. This is consistent with the results plotted in Figure 12(c) showing that the SF exhibits quite similar values when $\mu_r > 200$. The second element giving rise to an improved axial SF as the permeability decreases is the flux density profile around the sample. Figure 14 shows the distribution of the magnetic flux density as well as the magnetic flux lines when only superconducting material is considered (Figure 14(a)), only ferromagnetic material is considered (Figure 14(b)) and when both materials are considered (Figure 14(c)). When the only contribution comes from the superconducting material ($\mu_r = 1$), the flux density concentrates mainly close to the external lateral wall. As the value of μ_r increases and because of the anisotropy of the permeability, concentrations of the flux density also occur in the vicinity of the upper and lower surfaces which in turn, increases the penetration of the flux through the openings and thus decreases the shielding factor. As can be seen in Figure 14(a) and (c), the flux density profile inside the shield reveals a region in which the axial component of the flux density B_z cancels out. This region is spotted by the dash-dotted line at a radius R_0 and is characterised by a $SF > 1000$. According to the modelling results, far enough from the openings, this region forms a ring of radius $R_0 = 0.663R_{\text{in}}$ in the case HTS and $R_0 = 0.685R_{\text{in}}$ in the case FM+HTS. These values are quite close to the theoretical radius $R_0 = 0.628R_{\text{in}}$ expected for a type-I superconducting tube [1, 82].

6. Conclusion

In this work, we first investigated experimentally the ability of a stack of coated conductor annuli of large bore (26 mm inner diameter) to shield a magnetic field applied either along the axis of the stack (axial configuration) or, perpendicular to it (transverse configuration). The study was carried out on three samples with different heights at both room temperature and 77 K. The superconducting tapes combine a Ni-5at.%W ferromagnetic substrate and a (RE)BCO superconducting layer. At room temperature, the results are shown to be in a reasonable agreement with the analytical formulas applicable to purely ferromagnetic cylindrical shields. In particular, the ferromagnetic material allows for a shielding factor > 1 for both directions of the applied field. At 77 K, the superconducting layers mostly contribute to the shielding of the axial component of the applied magnetic field whereas the ferromagnetic substrates of the tapes mainly shield the transverse component. Numerical

homogenized models were implemented considering a field-dependent permeability $\mu_r(B)$ obtained by independent measurements on the same ferromagnetic substrates at both temperatures. The results are in very good agreement with the experimental measurements. Magnetic shielding measurements in axial field showed the ability of such stacks to shield magnetic flux densities up to 0.67 T where the shielding factor, decreasing with the applied field, is always > 3. Secondly, we show how these experimental results could be used to estimate the engineering critical current density J_e of the tapes, and the results were almost independent of the aspect ratio of the stack. Then, a numerical modelling of the shielding efficiency of stacks with different aspect ratios showed that at low fields, the SF is strongly influenced by the height of the stack i.e. SF increases from ~ 45 to > 30000 when the height is tripled. The practical consequence is that a stack of 72 mm height would be able to maintain a shielding factor exceeding 10 up to 0.931 T at 77 K. Finally, the effect of the critical current density and the magnetic permeability was investigated numerically. The J_c appears to have a finite but very weak effect on the transverse magnetic shielding. On the contrary, it strongly affects the axial shielding factor especially at $B_{\text{app}} > 100$ mT. Using a field-dependent $J_c(B)$ allows for a better agreement with the experimental results than using a constant critical current density. An increasing magnetic permeability was shown to be detrimental to the axial magnetic shielding and to improve the transverse shielding. The comparison between the experimental and the numerical results underlines the necessity to take into account the field dependence $\mu_r(B)$.

Acknowledgements

This work was supported by the Fonds de la Recherche Scientifique - FNRS under Grant CDR J.0218.20 (35325237). S. Brialmont is recipient of a grant from the Fonds pour la Formation à la Recherche dans l'Industrie et l'Agriculture (FRIA).

References

[1] Claycomb J R and Miller Jr J H 1999 *Rev. Sci. Instrum.* **70** 4562
[2] Pavese F 1998 *Magnetic shielding*, in: *Handbook of Applied Superconductivity* (Bristol Institute of Physics Publishing) pp 1461-83
[3] Bergen A *et al* 2016 *Rev. Sci. Instrum.* **87** 105109
[4] Arpaia P, Ballarino A, Giunchi G and Montenero G 2014 *J. Instrum.* **9** P04020
[5] Hinterberger A, Gerber S and Doser M 2017 *J. Instrum.* **12** T09002
[6] Jiles D 2015 *Introduction to Magnetism and Magnetic Materials*, 3rd Edition, (CRC Press, Taylor and Francis) 2015
[7] Takahata K, Nishijima S, Ohgami M, Okada T, Nakagawa S and Yoshiwa M 1989 *IEEE Trans. Magn.* **25** 1889
[8] Sasaki T and Itoh I 1996 *Cryogenics* **36** 497
[9] Rabbers J J, Oomen M P, Bassani E, Ripamonti G and Giunchi G 2010 *Supercond. Sci. Technol.* **23** 125003
[10] Fagnard J F, Elschner S, Bock J, Dirickx M, Vanderheyden B and Vanderbemden P 2010 *Supercond. Sci. Technol.* **23** 095012
[11] Wéra L, Fagnard J F, Namburi D K, Shi Y, Vanderheyden B and Vanderbemden P 2017 *IEEE Trans. Appl. Supercond.* **27** 6800305
[12] Gozzelino L *et al* 2020 *Supercond. Sci. Technol.* **33** 044018
[13] Takahashi K, Fujishiro H and Ainslie M D 2018 *Supercond. Sci. Technol.* **31** 044005
[14] Prigozhin L and Sokolovsky V 2018 *J. Appl. Phys.* **123** 233901
[15] Netter D, Lévêque J, Ailam E, Douine B, Rezzoug A and Masson P J 2005 *IEEE Trans. Appl. Supercond.* **15** 2186
[16] Douine B, Berger K and Ivanov N 2021 *Materials* **14** 1636
[17] Dorget R *et al* 2021 *Materials* **14** 2847
[18] Sugouchi R *et al* 2020 *IEEE Trans. Appl. Supercond.* **30** 3601905
[19] Barna D 2017 *Phys. Rev. Accel. Beams* **20** 041002
[20] Capobianco-Hogan K G *et al* 2018 *Nucl. Instrum. Methods Phys. Res. A* **877** 149
[21] Statera M *et al* 2018 *Nucl. Instrum. Methods Phys. Res. A* **882** 17
[22] Barna D *et al* 2022 *IEEE Trans. Appl. Supercond.* **32** 4000505
[23] Bortot L *et al* 2021 *Supercond. Sci. Technol.* **34** 105001
[24] Gozzelino L *et al* 2019 *Supercond. Sci. Technol.* **32** 034004
[25] Giunchi G, Barna D, Bajas H, Brunner K, Német A and Petrone C 2018 *IEEE Trans. Magn.* **28** 6801705
[26] Lousberg G, Fagnard J F, Ausloos M, Vanderbemden P and Vanderheyden B 2010 *IEEE Trans. Appl. Supercond.* **20** 33
[27] Gozzelino L, Gerbaldo R, Ghigo G, Laviano F and Truccato M 2017 *J. Supercond. Novel Magn.* **30** 749
[28] Fracasso M, Gömöry F, Solovyov M, Gerbaldo R, Ghigo G, Laviano F, Napolitano A, Torsello D and Gozzelino L 2022 *Materials* **15** 667
[29] Sasaki T, Tanaka M, Morita M, Miyamoto K and Hashimoto M 1992 *Jpn. J. Appl. Phys.* **31** 1026
[30] Yang P T, Yang W M and Chen J L 2017 *Supercond. Sci. Technol.* **30** 085003
[31] Yang P T, Fagnard J F, Vanderbemden P and Yang W M 2019 *Supercond. Sci. Technol.* **32** 115015
[32] Zhang Z Y, Matsumoto S, Teranishi R and Kiyoshi T 2012 *Phys. Procedia* **27** 180
[33] Gu C, Chen S, Pang T and Qu T M 2017 *Appl. Phys. Lett.* **110** 193505
[34] Kvitkovic J, Pamidi S and Voccio J 2009 *Supercond. Sci. Technol.* **22** 125009
[35] Kvitkovic J, Patel S, Zhang M, Zhang Z, Peetz J, Marney A and Pamidi S 2018 *IEEE Trans. Appl. Supercond.* **28** 9001705
[36] Kvitkovic J, Davis D, Zhang M and Pamidi S 2015 *IEEE Trans. Appl. Supercond.* **25** 8800304
[37] Tomków Ł, Ciszek M and Chorowski M 2015 *J. Appl. Phys.* **117** 043901
[38] Solovyov M, Šouc J, Gömöry F, Rikel M O, Mikulášová E, Ušáková M and Ušák E 2017 *IEEE Trans. Appl. Supercond.* **27** 8800204
[39] Solovyov M, Šouc J, Kucharovic M and Gömöry F, 2021 *IEEE Trans. Appl. Supercond.* **31** 4901205
[40] Fagnard J F, Dirickx M, Levin G A, Barnes P N, Vanderheyden B and Vanderbemden P 2010 *J. Appl. Phys.* **108** 013910
[41] Wéra L, Fagnard J F, Levin G, Vanderheyden B and Vanderbemden P 2015 *Supercond. Sci Technol.* **28**

074001
[42] Chi C *et al* 2020 *Supercond. Sci Technol.* **33** 095001
[43] Goyal A, Parans Paranthaman M and Schoop U 2004 *MRS Bull.* **29** 552
[44] de Boer B *et al* 2001 *Physica C* **351** 38
[45] Verebelyi D T *et al* 2003 *Supercond. Sci Technol.* **16** L19
[46] Miyagi D, Yunoki Y, Umabuchi M, Takahashi N and Tsukamoto O 2008 *Supercond. Sci Technol.* **468** 1743
[47] Claassen J H and Thieme C L H 2008 *Supercond. Sci Technol.* **21** 105003
[48] Statra Y, Menana H and Douine B 2021 *IEEE Trans. Appl. Supercond.* **31** 5900306
[49] Kvitkovic J, Patel S and Pamidi S 2017 *IEEE Trans. Appl. Supercond.* **27** 4700705
[50] Patel A, Baskys A, Mitchell-Williams T, McCaul A, Coniglio W, Hänisch J, Lao M and Glowacki B A 2018 *Supercond. Sci Technol.* **31** 09LT01
[51] Suyama M, Pyon S, Iijima Y, Awaji S and Tamegai T 2021 *Supercond. Sci Technol.* **34** 065004
[52] Zhou W, Staines M, Jiang Z, Badcock R A, Long N J, Buckley R G and Fang J 2018 *IEEE Trans. Appl. Supercond.* **28** 8200108
[53] Hahn S, Kim S B, Ahn M C, Voccio J, Bascuñán J and Iwasa Y 2010 *IEEE Trans. Appl. Supercond.* **20** 1037
[54] Kim S B, Kimoto T, Hahn S, Iwasa Y, Voccio J and Tomita M 2013 *Physica C* **484** 295
[55] Yuan X, Wang Y, Hou Y, Kan C, Cai C and Sun M 2018 *IEEE Trans. Appl. Supercond.* **28** 4603005
[56] Patel A, Hahn S, Voccio J, Baskys A, Hopkins S C and Glowacki B A 2017 *Supercond. Sci Technol.* **30** 024007
[57] Vanderbemden P, Wéra L, Fagnard J F, Vanderheyden B, Hahn S and Patel A, Presented at the *14th European Conference on Applied Superconductivity (EUCAS 2019)*, Glasgow, UK, 2-LO-OM-06S
[58] Peng Y, Zeng Z, Zhou D, Zhao W, Jia Z, Guo Y, Bai C, Fan F, Chen Y and Cai C 2021 *J. Supercond. Nov. Magn.* **34** 2493
[59] Grilli F *et al* 2005 *IEEE Trans. Appl. Supercond.* **15** 17
[60] Zhang M and Coombs T A 2012 *Supercond. Sci Technol.* **25** 015009
[61] Zemeño V M R and Grilli F 2014 *Supercond. Sci Technol.* **27** 044025
[62] Brambilla R, Grilli F, Martini L, Bocchi M and Angeli G 2018 *IEEE Trans. Appl. Supercond.* **28** 5207511
[63] Dular J, Geuzaine C and Vanderheyden B 2020 *IEEE Trans. Appl. Supercond.* **30** 8200113
[64] Dular J, Harutyunyan M, Bortot L, Schöps S, Vanderheyden B and Geuzaine C 2021 *IEEE Trans. Appl. Supercond.* **31** 8200412
[65] Dular J, Brialmont S, Vanderbemden P, Geuzaine C and Vanderheyden B *Finite Element Models for Magnetic Shields made of Stacked Tapes*, presented at the *8th International Workshop on Numerical Modelling of High Temperature Superconductors*, Nancy, 2022
[66] Wang J, Lin H, Huang Y and Sun X 2011 *IEEE Trans. Magn.* **35** 1378-1381
[67] Hahn S, Voccio J, Park D K, Kim K M, Tomita M, Bascuñán J and Iwasa Y 2012 *IEEE Trans. Appl. Supercond.* **22** 4302204
[68] Jackson J D 1999, *Classical Electrodynamics*. College Park, MD, USA: Amer. Assoc. Phys. Teachers.
[69] Brialmont S, Fagnard J F, Vanderheyden B, Mazaleyrat F, Hahn S, Patel A and Vanderbemden P 2022 *IEEE Trans. Appl. Supercond.* **32** 6602710
[70] Rhyner J 1993 *Physica C: Supercond.* **212** 292-300
[71] Life-HTS: Liege University Finite Element Models for High-Temperature Superconductors, http://www.life-hts.uliege.be/
[72] GetDP: A General Environment for the Treatment of Discrete Problems, https://getdp.info/
[73] Mager A 1968 *J. Appl. Phys.* **39** 1914
[74] Mager A J 1970 *IEEE Trans. Magn.* **6** 67
[75] Chen D X, Pardo E and Sanchez A 2006 *J. Magn. Magn. Mater.* **306** 135-136
[76] Sridhar S, Wu D H, Kennedy W 1989 *Phys. Rev. Lett.* **63** 1873-1876
[77] Brandt E H 2001 *Phys. Rev. B* **64** 024505
[78] Mawatari Y 1996 *Phys. Rev. B* **54** 215-221
[79] Orlando T P and Delin K A, "Foundations of Applied Superconductivity", *Addison-Wesley*, 1991
[80] Cabrera B 1975, *The Use of Superconducting Shields for Generating Ultra Low Magnetic Field Regions and Several Related Experiments*, PhD Thesis, Stanford University
[81] Navau C, Sanchez A, Pardo E, Chen D X, Bartholomé E, Granados X, Puig T and Obradors X 2005 *Phys. Rev. B* **71** 214507
[82] Fagnard J F, Vanderheyden B, Pardo E and Vanderbemden P 2019 *Supercond. Sci. Technol.* **32** 074007